Effect of ozone sensitization on the reflection patterns and stabilization of standing detonation waves induced by curved ramps

Eric J. Ching[a], Ryan F. Johnson[a]

[a]*Laboratories for Computational Physics and Fluid Dynamics, U.S. Naval Research Laboratory, 4555 Overlook Ave SW, Washington, DC 20375*

Abstract

Standing detonation engines are a promising detonation-based propulsion technology. The most commonly studied standing detonation configuration involves a straight-sided wedge that induces an oblique detonation wave. A recently introduced standing-detonation-engine concept entails a curved ramp that leads to formation of a curved detonation wave. The continuous compression or expansion induced by the ramp curvature can have significant influence on the flow characteristics and wave patterns of the detonation wave, offering greater flexibility in engine design than conventional wedge geometries. This study aims to further explore this relatively new standing-detonation-engine concept by examining the effect of ignition promoters, namely ozone, on the flow characteristics and reflection patterns of curved detonation waves induced by convex or concave ramps inside a confined combustion chamber. Simulations are performed using a positivity-preserving and entropy-bounded discontinuous Galerkin method with curved elements to exactly represent the ramp geometries. In the context of wedge-induced oblique detonation waves, ozone addition has been found to decrease the initiation length and lead to a smoother shock-detonation transition. This can then attenuate the detonation and reduce stagnation-pressure losses, thus improving the potential propulsion performance. In the context of detonation waves induced by curved ramps, although ozone addition similarly shortens the initiation zone, the curvature of the ramp introduces additional effects that can amplify or counteract both the ozone-induced contraction of the initiation zone and the aforementioned detonation attenuation. For example, in the case of convex walls, the reduced initiation length causes shock-detonation transition to occur at a steeper ramp angle, where the curved leading shock is stronger. As a result, the curved detonation wave can actually be strengthened, which is detrimental to detonation stabilization (in the case of a Mach reflection pattern) and stagnation-pressure recovery. However, the initiation zone is shortened to a greater degree than in the case of concave ramps since it no longer spans the shallower downstream portion of the ramp. Conversely, in the case of concave walls, the smaller initiation zone causes transition to occur at a shallower ramp angle, where the leading shock is weaker. The attenuation of the detonation can then be magnified, further reducing stagnation-pressure losses and improving detonation stabilization (in the case of a Mach reflection pattern), although the initiation length is decreased to a smaller extent than in the case of convex ramps since the initiation zone becomes restricted to shallower ramp angles. Finally, we present specific examples wherein ozone addition changes the type of reflection pattern (e.g., regular reflection, stationary Mach reflection, and non-stationary Mach reflection).

Keywords: Detonation; ozone; fuel sensitization; hypersonic flow

1. Introduction

Detonation waves are supersonic combustion phenomena characterized by a shock wave followed by a smooth, closely coupled combustion region. The high temperature behind the shock ignites the mixture,

---

which reacts rapidly to the equilibrium state and leads to an energy release that in turn drives the motion of the shock. Propulsion and power systems based on detonation have emerged as a promising technology for hypersonic flight, space travel, and reduced emissions due to higher thermodynamic and combustion efficiencies and simpler geometric structure than traditional deflagration-based systems [1, 2]. A number of detonation-based engine concepts exist, including rotating detonation engines [3, 4], pulse detonation engines [2, 5], and standing detonation engines [6, 7]. Standing detonation engines are appealing due to their simple and economical design and their theoretical applicability to a wide range of flight Mach numbers.

The most conventional standing-detonation-engine concept involves high-speed flow past a fixed wedge, resulting in the formation of an oblique detonation wave (ODW). For such wedge-induced ODWs, an oblique shock wave (OSW) first forms at the leading edge, compressing and heating the mixture before transitioning to an ODW. However, a major challenge associated with this engine concept is reliable detonation initiation and stabilization. In order to achieve a stable ODW, the wedge angle must be large enough to obtain a complete detonation but small enough to prevent detachment of the ODW [8]. The difficulty of sustaining a detonation is exacerbated in experiments due to the limited run times of most facilities. In an important breakthrough in 2021, Rosato et al. [7] experimentally stabilized an ODW at relevant conditions for approximately three seconds by using a converging-diverging nozzle to sustain hypersonic flow at Mach 5.

The majority of studies in the literature that investigate ODW initiation and stabilization or the underlying physics of ODWs rely on numerical simulations. Early analyses of ODWs approximated the detonation wave as an OSW coupled with instantaneous post-shock heat release [8]. However, it has since been determined that there exists a nonreactive initiation zone between the OSW and ODW [9, 10]. There are two types of OSW-to-ODW transition mechanisms: *abrupt* transition and *smooth* transition [11, 12, 13], each associated with a complex wave structure. In the former, which occurs at lower Mach numbers, the leading OSW and ODW intersect at a multi-wave point. In the latter, which is favorable for detonation stabilization, the multi-wave point is replaced with a curved-shock region. Hysteresis associated with OSW-to-ODW transition has also been investigated [14]. Other studies have examined the cellular structure characterizing the ODW front [15, 16, 17]. In particular, the ODW front comprises three zones: the first is characterized by ZND-type detonation without any cellular structure, the second contains left-running transverse waves, and the third consists of both left-running and right-running transverse waves, giving rise to a cellular structure similar to that observed in multi-headed normal detonations. The existence of microscopic hypersonic jets ("micro-jets") in the third zone has also been observed [18].

The addition of ozone and other ignition promoters to the incoming fuel-air mixture has recently been explored as a means to improve the stabilization characteristics of ODWs. This is motivated by the fact that ozone addition can accelerate ignition and reduce the induction length in ZND calculations due to increased production of O radicals [19]. Additionally, experiments performed by Crane et al. [20] demonstrated that ozone doping can significantly reduce detonation cell size, and the thermodynamic properties of the mixture (e.g., Chapman-Jouguet speed, post-shock state, and equilibrium state) are largely unaffected. In the context of ODWs, Teng et al. [21] found that ozone addition can significantly decrease initiation length and change abrupt ODW transitions to smooth transitions, improving ODW stabilization characteristics and allowing for reduced combustor sizes. The decrease in initiation length is more pronounced at lower Mach numbers. The reason for the change in transition mechanism is that the shorter initiation length suppresses the convergence of compression waves into shocks, promoting smooth transitions. Analyses of total-pressure losses revealed that ozonated ODWs exhibit improved propulsion performance. Vashishtha et al. [22] performed similar studies and reached the same qualitative conclusions, though they also examined the effect of H_2O_2 (another ignition promoter) addition and found that H_2O_2 doping is more effective than O_3 doping at higher Mach numbers associated with smooth ODW transitions.

Apart from ODWs induced by straight-sided wedges, ODWs induced by other geometries, such as cones [23, 24, 25], truncated cones [26], and double wedges [27], have been investigated. Xiang et al. [28] considered a wedge that then transitions into a curved surface, and Xiong et al. [29] and Yan et al. [30] examined curved detonation waves (CDWs) induced by curved ramps[1]. In [30], the stabilization character-
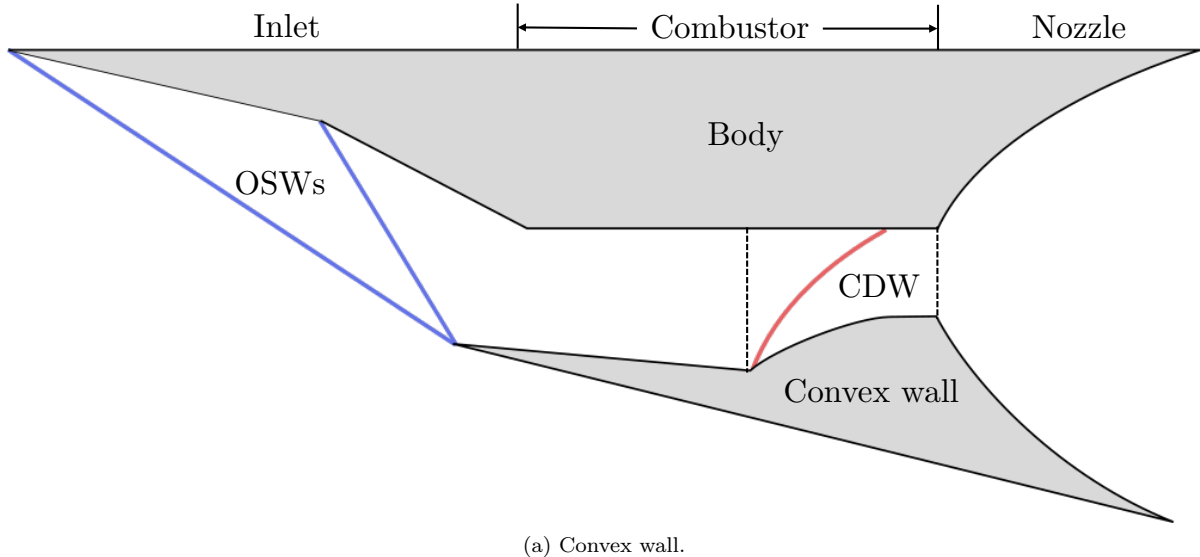
---

[1]Although straight-sided wedges can give rise to detonations with a curved shape [30], in this paper, a curved detonation wave (CDW) refers specifically to a detonation induced by a curved wall.
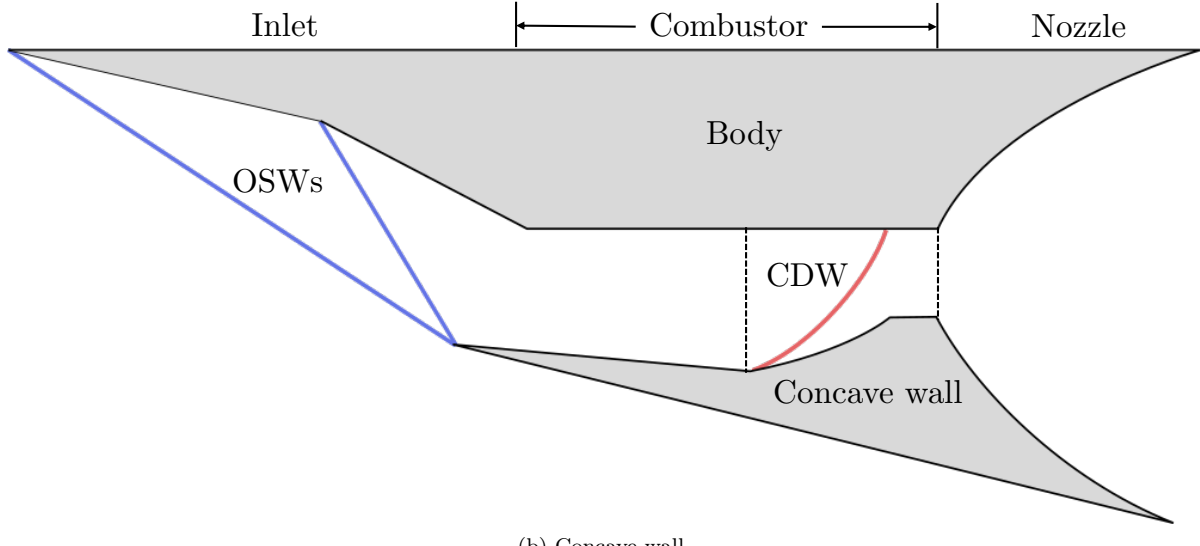
istics and reflection patterns of hydrogen-oxygen CDWs in two types of confined combustion chambers were investigated: the first with a convex ramp and the second with a concave ramp. Note that in computational studies of ODWs, chamber confinement is often neglected (i.e., a semi-infinite wedge is assumed), although a number of studies have considered a confined chamber [31, 32]. The effect of the degree of curvature was of particular interest. A simple quantitative criterion for obtaining a stationary CDW was also developed. Three broad types of reflection patterns were observed: (a) non-stationary Mach reflection, which occurs if the curvature is too high due to the presence of high-pressure, subsonic regions that interact and merge; (b) stationary Mach reflection, which occurs as the curvature is decreased; (c) stationary regular reflection, which is the most favorable in terms of stability. The use of curved ramps can significantly affect detonation initiation and stabilization. For example, in the case of convex walls, the steepness of the leading edge can reduce the initiation length compared to the case of a straight-sided wedge with the same endpoints. In addition, the continuous expansion caused by the convex surface can attenuate the detonation, potentially decreasing the likelihood of a non-stationary Mach reflection and reducing stagnation-pressure losses [29]. On the other hand, continuous compression induced by concave walls can facilitate combustion. A ramp that changes in convexity can exploit both the expansion and compression caused by convex and concave surfaces, respectively, further improving detonation initiation and stabilization [29, 30] (though this concept has yet to be explored in detail).

Given the potential of both ozone doping and the use of curved walls, this work aims to investigate the effect of ozone addition on the reflection patterns and flow characteristics of standing hydrogen-oxygen CDWs induced by curved ramps. In particular, we consider a similar geometric configuration to that in [30] (i.e., a confined combustion chamber with either a convex ramp or a concave ramp), as displayed in Figure 1.1. We examine how ozone sensitization affects detonation initiation and the resulting Mach-reflection and regular-reflection patterns at various curvatures. The effect of ozone addition on stagnation-pressure losses is also of interest. The findings of this study will improve understanding of the effects of ignition promoters on this relatively new standing-detonation-engine concept.

The remainder of this article is organized as follows. The governing equations, associated physical models, and discretization techniques are discussed in Section 2. The following section presents the results and corresponding discussion. The paper then concludes with some final remarks.

(a) Convex wall.

(b) Concave wall.

Figure 1.1: Representative schematic of a standing detonation engine with a convex ramp and a concave ramp. The region enclosed by the dashed lines represents the computational domain. OSW: oblique shock wave. CDW: curved detonation wave.

2. Physical and mathematical modeling

2.1. Governing equations and numerical methods

The governing equations are the compressible, multicomponent, chemically reacting Euler equations in two spatial dimensions. As in related studies [22, 21, 29, 30], viscous effects are neglected. These equations are written as

$$\frac{\partial y}{\partial t} + \nabla \cdot \mathcal{F}(y, \nabla y) - \mathcal{S}(y) = 0, \tag{2.1}$$

where y is the state vector, t is time, $\mathcal{F}$ is the convective flux, and $\mathcal{S} = (0, \ldots, 0, 0, \omega_1, \ldots, \omega_{n_s})^T$ is the chemical source term, with ω_i corresponding to the production rate of the ith species. The physical coordinates are denoted by $x = (x_1, x_2)$. The vector of state variables is expanded as

$$y = (\rho v_1, \rho v_2, \rho e_t, C_1, \ldots, C_{n_s})^T, \tag{2.2}$$

where ρ is density, $v = (v_1, v_2)$ is the velocity vector, e_t is the specific total energy, $C = (C_1, \ldots, C_{n_s})$ is the vector of molar concentrations, and n_s is the number of species. The partial density of the ith species is defined as

$$\rho_i = W_i C_i,$$

where W_i is the molecular weight of the ith species, from which the density can be computed as

$$\rho = \sum_{i=1}^{n_s} \rho_i.$$

The mole and mass fractions of the ith species are given by

$$X_i = \frac{C_i}{\sum_{i=1}^{n_s} C_i}, \quad Y_i = \frac{\rho_i}{\rho}.$$

The equation of state for the mixture is written as

$$P = R^0 T \sum_{i=1}^{n_s} C_i, \tag{2.3}$$

where P is the pressure, T is the temperature, and R^0 is the universal gas constant. The specific total energy is the sum of the mixture-averaged specific internal energy, u, and the specific kinetic energy, written as

$$e_t = u + \frac{1}{2} \sum_{k=1}^{d} v_k v_k,$$

where the former is the mass-weighted sum of the specific internal energies of each species, given by

$$u = \sum_{i=1}^{n_s} Y_i u_i.$$

Assuming a thermally perfect gas, u_i is defined as

$$u_i = h_i - R_i T = h_{\text{ref},i} + \int_{T_{\text{ref}}}^{T} c_{p,i}(\tau) d\tau - R_i T,$$

where h_i is the specific enthalpy of the ith species, $R_i = R^0/W_i$, T_{ref} is the reference temperature of 298.15 K, $h_{\text{ref},i}$ is the reference-state species formation enthalpy, and $c_{p,i}$ is the specific heat at constant pressure of the ith species, which is approximated with a polynomial as a function of temperature based on the NASA coefficients [33, 34]. The kth spatial component of the convective flux is written as

$$\mathcal{F}_k^c(y) = (\rho v_k v_1 + P\delta_{k1}, \ldots, \rho v_k v_d + P\delta_{kd}, v_k(\rho e_t + P), v_k C_1, \ldots, v_k C_{n_s})^T. \tag{2.4}$$

We employ detailed chemical kinetics based on the H_2 sub-model of the Foundational Fuel Chemistry Model Version 1.0 (FFCM-1) [35] combined with the Princeton ozone sub-model [36].

The governing equations are spatially discretized using a positivity-preserving and entropy-bounded discontinuous Galerkin method that can guarantee nonnegative species concentrations, positive density, positive temperature, and bounded specific entropy (from below) [37, 38]. Overintegration techniques to reduce spurious pressure oscillations in smooth regions of the flow are applied [39]. Strang splitting is employed to deal with the stiff chemical source term, where second-order strong-stability-preserving Runge-Kutta time integration [40, 41] is used for the transport step and an implicit DG discretization in time is

used for the reaction step. All simulations in this work are performed using a $p = 1$ solution approximation, where p denotes the polynomial degree (with an order of accuracy of $p + 1$ in smooth regions), and a $p = 2$ geometric approximation. To minimize numerical artifacts at discontinuities, an artificial-viscosity term

$$\nabla \cdot (\nu_{\text{AV}} \nabla y) \tag{2.5}$$

is added to the RHS of Equation (2.1), where the artificial viscosity, ν_{AV}, is computed as

$$\nu_{\text{AV}} = C_{\text{AV}} S_{\text{AV}} \left(\frac{h^2}{p+1} \right).$$

C_{AV} is a user-defined parameter, S_{AV} is a shock sensor based on pressure variations inside a given element [42], and h is a length scale associated with the element. ν_{AV} is then made C^0-continuous as in [43]. The artificial-viscosity term (2.5) is discretized using the SIPG viscous flux function [44].

2.2. Computational setup

Two types of computational domains, as shown in Figure 2.1 are considered in this work. The overall dimensions of the combustion chamber are similar to those in [30], which were based on [32] and [31], although a significant portion of the freestream region is neglected here for computational savings. For consistency with [30], the chamber is inverted in the vertical direction, and $x_{2,c}$ is the ramp profile, which is a quadratic function of x_1. Figure 2.1a displays a concave ramp, while Figure 2.1b displays a convex ramp. In Section 3, Points A and B are fixed, Point C is varied in the x_1-direction to obtain different curvatures, and the remaining points are modified to enlarge/reduce the domain as needed. α_1 and α_2 in Figure 2.1 are the initial and final angles of the ramp, respectively. Following [30], the mean curvature is defined as

$$\kappa = \frac{\Delta\alpha}{s} = \frac{\alpha_2 - \alpha_1}{s},$$

where s is the arc length of the curved ramp (i.e., Curve BC). Note, however, that κ, while an important parameter, does not by itself capture all relevant information about the ramp geometry.

(a) Concave wall. $A = (-5, 100), B = (0, 100), D = (210, 62), E = (210, 0), F = (125, 0), G = (125, 15), H = (60, 70)$.

(b) Convex wall. $A = (-5, 100), B = (0, 100), D = (210, 62), E = (210, 0), F = (120, 0)$.
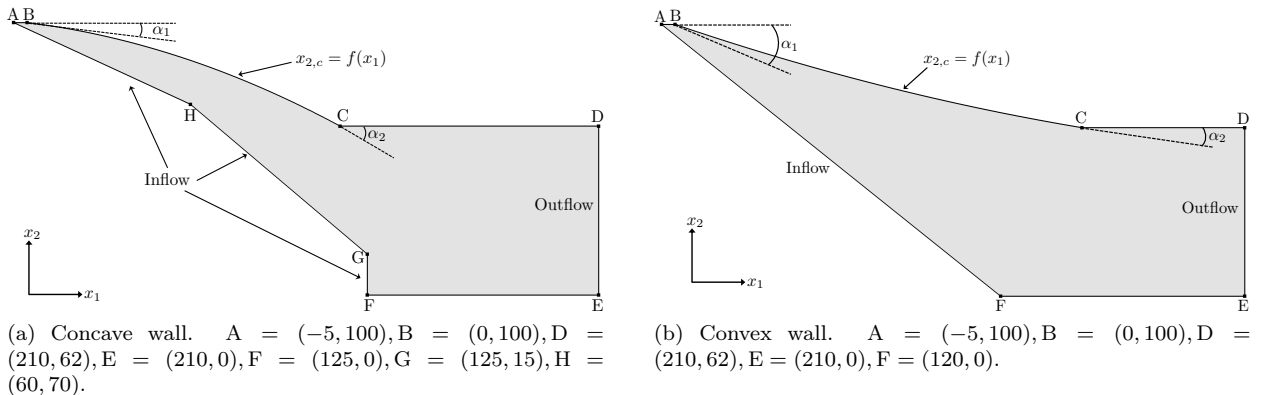
Figure 2.1: Computational domains with (a) concave wall and (b) convex wall. α_1 and α_2 are the initial and final angles, respectively, of the wall. Point C is varied to obtain different mean curvatures. The point coordinates are in units of mm.

As in [30], the state at the inflow boundaries in Figure 2.1 is fully prescribed as $v_1 = 2495$ m/s, $P = 1$ bar, $T = 700$ K, and a lean hydrogen-air mixture at an equivalence ratio of 0.34. These conditions roughly correspond to Mach 9 flow at a temperature and pressure of 200 K and 6 kPa, respectively, after compression by a $25°$ OSW. The inflow state is the initial condition as well. Extrapolation is applied at the outflow boundary, and slip-wall conditions are imposed on the remaining boundaries in Figure 2.1. Similar to [30],

6

ozone is added to the mixture in the following amounts: 0, 1000, and 10,000 ppm (by mole). Gmsh [45] is used to generate unstructured triangular meshes with a characteristic element size of $h = 0.1$ mm. Information on grid convergence is provided in Appendix A. Note that with a $p = 1$ solution approximation, each triangular element has three degrees of freedom (per state variable), and with a $p = 2$ geometric approximation, the walls are exactly represented since $x_{2,c}$ is a quadratic function of x_1.

3. Results and discussion

ZND calculations performed with the Shock Detonation Toolbox [46] are first presented in order to qualitatively examine the effect of ozone addition in the simplified one-dimensional setting. Results for concave walls are then discussed, followed by those for convex walls. All simulations in Sections 3.2 and 3.3 are performed using a modified version of the JENRE® Multiphysics Framework [39] that incorporates the extensions described in [37, 38] and in Section 2.

3.1. ZND calculations

The initial, pre-shock state is set as the inflow state (with no ozone, 1000 ppm ozone, or 10,000 ppm ozone) described in Section 2.2. Chapman-Jouguet conditions are assumed. Figure 3.1 presents the profiles of temperature, pressure, and stagnation-pressure recovery (SPR), which is defined as the ratio between the (local) stagnation pressure and the inflow stagnation pressure. This quantity is an approximate measure of the propulsion performance [29, 21]. The region $x < 0$ mm corresponds to the initial, pre-shock state, and the shock is located at $x = 0$ mm. In Figure 3.1c, the initial state, where SPR is simply unity, is not shown. Ozone addition reduces the induction length and increases the temperature and pressure behind the shock. The ozone-induced increase in temperature behind the induction zone is more noticeable than the ozone-induced increase in pressure. SPR is decreased as a result of ozone sensitization. The overall changes in post-shock temperature, pressure, and SPR due to ozone, however, are not significant. The difference between 1000 ppm ozone and 10,000 ppm ozone is greater than that between no ozone and 1000 ppm.
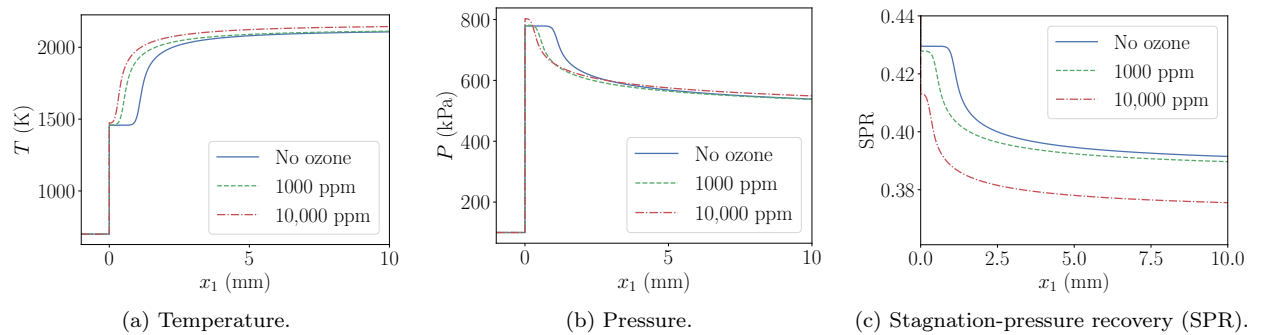

| (a) Temperature. | (b) Pressure. | (c) Stagnation-pressure recovery (SPR). |

Figure 3.1: Temperature, pressure, and SPR profiles from ZND calculations at Chapman-Jouguet conditions.

3.2. Concave walls

This section presents results for four concave cases, as listed in Table 1. α_1 is fixed across all cases, and Point C in Figure 2.1a is varied in the x_1-direction to obtain different curvatures. As indicated in the fifth column of Table 1, the letter refers to the ozone amount (e.g., Case 1A corresponds to $\kappa = 3.05$ km^{-1} and no ozone). Stationary Mach reflections are observed in all cases except Case 2C, which corresponds to a regular reflection, and Case 4A, which corresponds to a non-stationary Mach reflection.

Table 1: Geometric information for concave ramp. Units are in mm unless otherwise specified.

Case	Point C	Wall profile	κ $\left(\text{km}^{-1}\right)$	Ozone	Reflection pattern
1	$(115, 62)$	$x_{2,c} = -0.001805x_1^2 - 0.1229x_1 + 100$	3.05	1A: 0 ppm 1B: 1000 ppm 1C: 10,000 ppm	1A: Mach reflection 1B: Mach reflection 1C: Mach reflection
2	$(134, 62)$	$x_{2,c} = -0.001199x_1^2 - 0.1229x_1 + 100$	2.12	2A: 0 ppm 2B: 1000 ppm 2C: 10,000 ppm	2A: Mach reflection 2B: Mach reflection 2C: Regular reflection
3	$(90, 62)$	$x_{2,c} = -0.003326x_1^2 - 0.1229x_1 + 100$	5.09	3A: 0 ppm 3B: 1000 ppm 3C: 10,000 ppm	3A: Mach reflection 3B: Mach reflection 3C: Mach reflection
4	$(84, 62)$	$x_{2,c} = -0.003922x_1^2 - 0.1229x_1 + 100$	5.80	4A: 0 ppm 4B: 1000 ppm 4C: 10,000 ppm	4A: Non-stationary 4B: Mach reflection 4C: Mach reflection

3.2.1. Case 1

Figures 3.2 and 3.3 present the temperature and pressure fields, respectively, for Cases 1A, 1B, and 1C at $t = 1.88$ ms, which is sufficient time for the CDW to stabilize. Table 2 lists the x_1-coordinates of the points of transition from the leading shock wave (LSW) to the CDW, as well as the percent difference with respect to the ozone-free case. An abrupt transition occurs in all cases, characterized by compression waves that converge into a transitional detonation that then intersects the LSW, CDW, and primary slip line at the transition point. The addition of ozone noticeably shortens the initiation zone and causes the transition point to move upstream, where the LSW is weaker as a result of the wall concavity. Consequently, the angle of the detonation wave is shallower, leading to lower temperatures and pressures behind the detonation and reflected shock. The height of the Mach stem is then decreased. The transitional detonation and associated transverse and reflected waves weaken as the ozone concentration is increased. Note that even in the case of a straight-sided wedge, initation-length reduction due to ozone addition can attenuate the detonation by mitigating the coalesence of compression waves near the reaction front [21], especially if the shock-detonation transition changes from abrupt to smooth (not the case here); with a concave ramp, the detonation is further attenuated by the weaker LSW as the transition point moves upstream. The ozone-induced contraction of the initiation zone, however, is somewhat offset by, as observed in Figures 3.2 and 3.3, the lower upstream temperatures and pressures ahead of the reaction front (due to a shallower ramp angle), which normally have the competing effect of induction-zone enlargement. This will be further confirmed in Section 3.3, where convex ramps are considered. In Case 1A (no ozone), a transverse wave noticeably interacts with the expansion fan. In Cases 1B and 1C, a transverse wave intersects the reflected shock and reflects off the secondary slip line. The difference between Cases 1A and 1B is greater than that between Cases 1B and 1C.
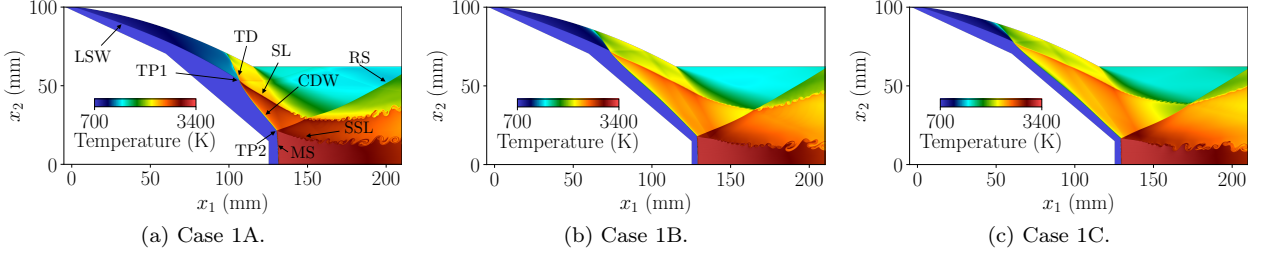
Figure 3.2: Temperature fields for Cases 1A, 1B, and 1C. LSW: leading shock wave. TP1: transition point. TD: transitional detonation. CDW: curved detonation wave. SL: slip line. RS: reflected shock. MS: Mach stem. SSL: secondary slip line. TP2: secondary triple point.
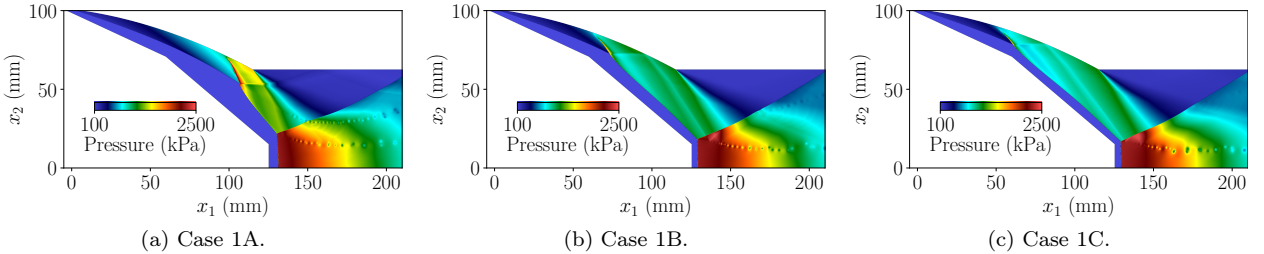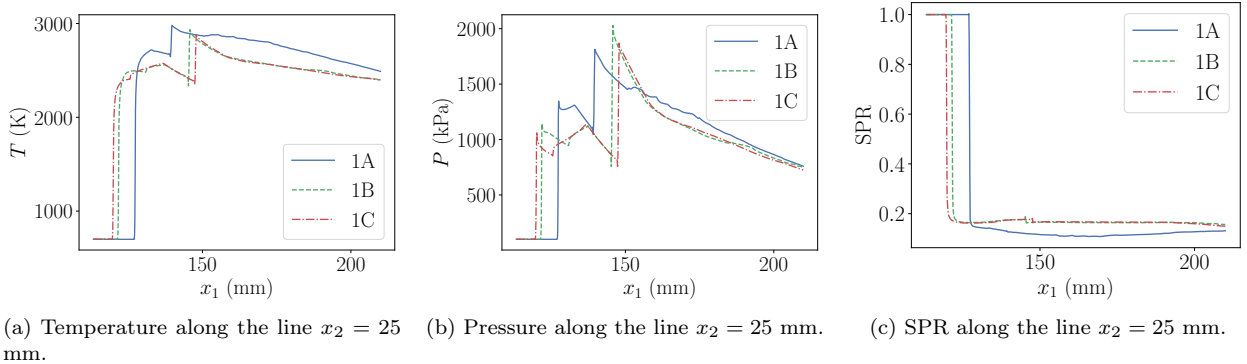

Figure 3.3: Pressure fields for Cases 1A, 1B, and 1C.

Table 2: x_1-coordinates of LSW-CDW transitions for Case 1 (concave).

Case	Ozone addition	LSW-CDW transition	Relative change vs. Case 1A
1A	0 ppm	$x_1 \approx 107$ mm	0%
1B	1000 ppm	$x_1 \approx 73$ mm	32%
1C	10,000 ppm	$x_1 \approx 61$ mm	43%

Figures 3.4a and 3.4b show the variation of temperature and pressure along the line $x_2 = 25$ mm, which intersects the CDW and reflected shock. The first large temperature and pressure jump is due to the CDW, which is positioned further upstream with ozone addition. Small variations in temperature and pressure then occur as a result of transverse waves. The second large jump in temperature and pressure is due to the reflected shock, which is moved downstream with ozone addition. Expansion continues to occur behind the reflected shock. The temperature increase across the CDW is greatest in Case 1A, but the reflected shock is stronger in the case of ozone sensitization. The combined effects of a shorter initiation length and weaker shock at the point of transition, both of which attenuate the CDW, lead to higher-Mach-number flow behind the CDW and consequently a stronger reflected shock. Note that the smaller temperature and pressure increase across the CDW with ozone addition is in qualitative contrast with the ZND calculations discussed in Section 3.1, which is, as previously mentioned, a consequence of smoothening of the shock-detonation transition (even though it remains abrupt) and a weaker LSW as the transition point moves upstream.

9

(a) Temperature along the line $x_2 = 25$ mm.

(b) Pressure along the line $x_2 = 25$ mm.

(c) SPR along the line $x_2 = 25$ mm.

Figure 3.4: Variation of temperature, pressure, and SPR along the line $x_2 = 25$ mm for Case 1 (concave).

The SPR distributions for all cases are given in Figure 3.5. The stronger compression at the reaction front in Case 1A leads to higher SPR above the slip line than in Cases 1B and 1C (note that due to the vertically inverted combustion chamber, this region would traditionally considered to be "below" the slip line). Behind the reaction zone above the slip line, the stagnation pressure first increases away from the wall and then decreases close to the slip line. This initial increase in SPR is caused by coalescence of the compression waves [29], which is then counteracted by weaker SPR ahead of the transitional detonation caused by a steeper LSW angle. The stagnation-pressure loss is greatest across the Mach stem. SPR across the CDW improves as the ozone concentration increases, which is further illustrated in the SPR variation along the line $x_2 = 25$ mm in Figure 3.4c. The SPR only slightly decreases across the reflected shock.
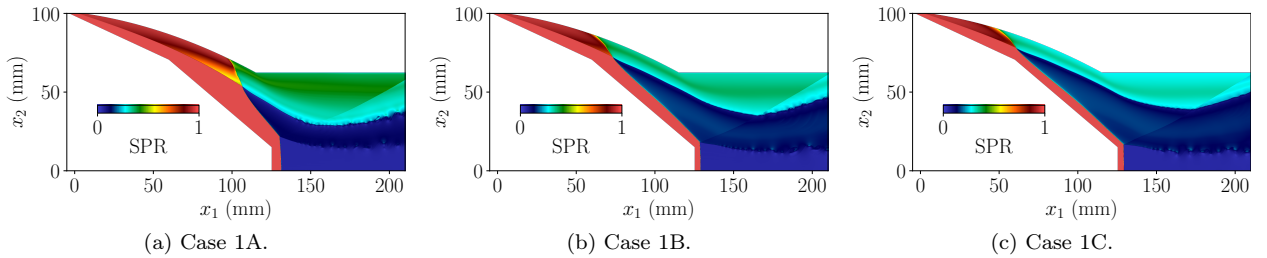

(a) Case 1A.

(b) Case 1B.

(c) Case 1C.

Figure 3.5: SPR distributions for Cases 1A, 1B, and 1C.

.

3.2.2. Case 2

Here, Point C is moved downstream, resulting in a reduced curvature of $\kappa = 2.12$ km^{-1}. The temperature and pressure fields at $t = 1.57$ ms, which is sufficiently long to reach quasi-steady detonation, are displayed in Figures 3.6 and 3.7. The x_1-coordinates of the LSW-CDW transitions for each case are given in Table 3. A Mach reflection pattern is observed in Cases 2A and 2B, while a regular reflection is observed in Case 2C (10,000 ppm of ozone). Abrupt LSW-CDW transitions occur in all cases. The addition of ozone significantly shortens the initiation zone and moves the transition point upstream, even moreso than in Case 1, which corresponds to a larger curvature and smaller initiation zone. Without ozone, the convergence of compression waves into a transitional detonation takes place near the tail of the ramp. As a result, transverse waves do not reflect off the curved ramp, as they do in Cases 2B and 2C. Additionally, in Case 2A, the expansion fan mitigates the coalescence of compression waves, leading to a small low-temperature, nonreactive region immediately behind the expansion corner. The transitional detonation is also stronger in Case 2A. The region behind the CDW bounded by the slip line and reflected shock is significantly smaller in the absence

of ozone. In Case 2C, the slip line and reflected shock do not intersect before the end of the domain. Since the transition point in Case 2A is located near the tail of the ramp, the post-CDW flow directly interacts with the expansion fan stemming from the convex corner, almost immediately decreasing in pressure and turning towards the x_1-direction. In contrast, since the transition points in Cases 2B and 2C are located further upstream, the flow behind the reaction front and CDW first undergoes continuous compression due to the ramp concavity before reaching the expansion fan. Furthermore, just as in Case 1, with ozone addition, the smaller initiation zone spans shallower ramp angles and thus reduced compression, attenuating the CDW and mitigating the ozone-induced decrease in initiation length. The relative change in the transition locations is greater here than in the higher-curvature Case 1.

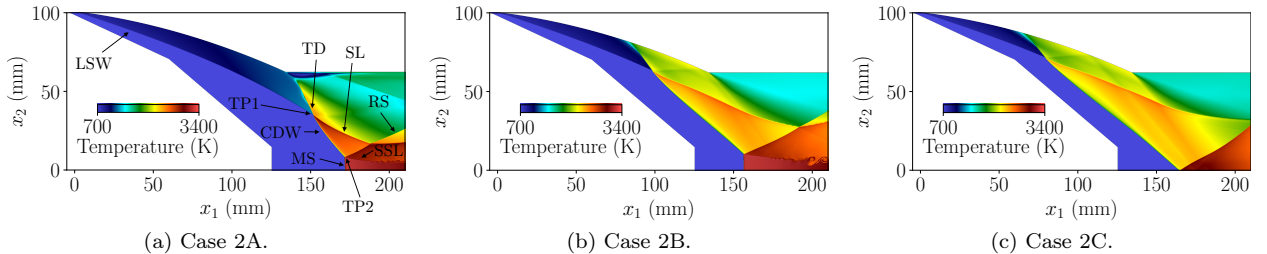(a) Case 2A. (b) Case 2B. (c) Case 2C.

Figure 3.6: Temperature fields for Cases 2A, 2B, and 2C. LSW: leading shock wave. TP1: transition point. TD: transitional detonation. CDW: curved detonation wave. SL: slip line. RS: reflected shock. MS: Mach stem. SSL: secondary slip line. TP2: secondary triple point.
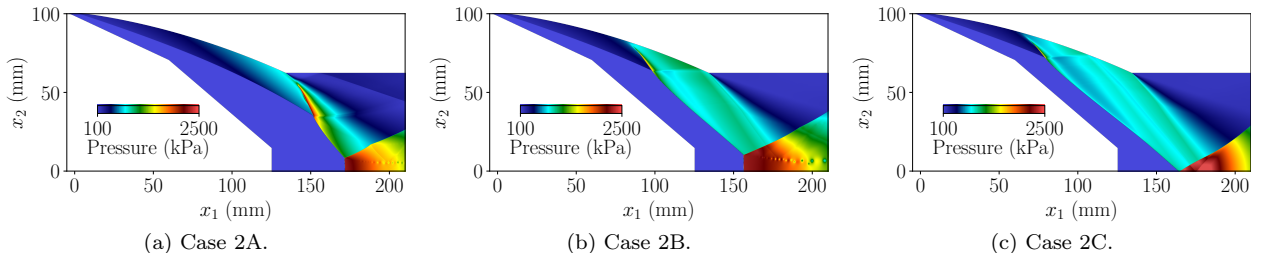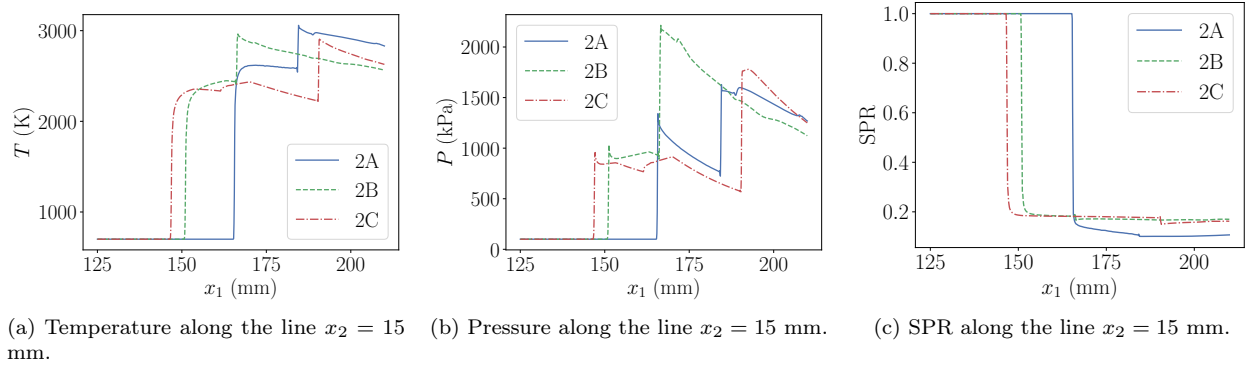

(a) Case 2A. (b) Case 2B. (c) Case 2C.

Figure 3.7: Pressure fields for Cases 2A, 2B, and 2C.

Table 3: x_1-coordinates of LSW-CDW transitions for Case 2 (concave).

Case	Ozone addition	LSW-CDW transition	Relative change vs. Case 2A
2A	0 ppm	$x_1 \approx 152$ mm	0%
2B	1000 ppm	$x_1 \approx 98$ mm	36%
2C	10,000 ppm	$x_1 \approx 79$ mm	48%

Figures 3.8a and 3.8b show the temperature and pressure along the line $x_2 = 15$ mm, which intersects the CDW and reflected shock. The temperature and pressure jumps across the CDW are lowest in Case 2C. This is again due to the smaller initiation zone, which smoothens the LSW-CDW transition (even though it is still abrupt), combined with the reduced ramp angle and therefore weaker LSW as the transition is moved upstream. This weaker CDW in Case 2C leads to faster, less deflected flow behind the CDW, resulting in a stronger reflected shock, as indicated by the greater temperature and pressure jumps near the outflow boundary, and suppressing the formation of a Mach stem. The CDW is positioned furthest upstream in

11

Case 2C, and the lack of a Mach stem causes the reflected shock to intersect the line $x_2 = 15$ mm further downstream than Cases 2A and 2B. In all cases, significant flow expansion is observed behind the reflected shock, and the small variations in pressure are caused by transverse and reflected waves. Overall, the influence of ozone sensitization is qualitatively similar to that in the higher-curvature Case 1, although magnified here due to the very large initiation zone in the absence of ozone.

(a) Temperature along the line $x_2 = 15$ mm.

(b) Pressure along the line $x_2 = 15$ mm.

(c) SPR along the line $x_2 = 15$ mm.

Figure 3.8: Variation of temperature, pressure, and SPR along the line $x_2 = 15$ mm for Case 2 (concave).

As indicated in the SPR distributions presented in Figure 3.9, the SPR behind the reaction zone above the slip line is overall higher in the absence of ozone, just as in Case 1. The greatest stagnation-pressure losses are due to the Mach stem, which is completely avoided in Case 2C (10,000 ppm of ozone). The SPR across the CDW is improved with the addition of ozone, as further illustrated in Figure 3.8c. The stronger reflected shock in Case 2C causes a greater loss in stagnation pressure than in Case 2B, such that the SPR in Case 2C is slightly lower at the outflow boundary in Figure 3.8c.
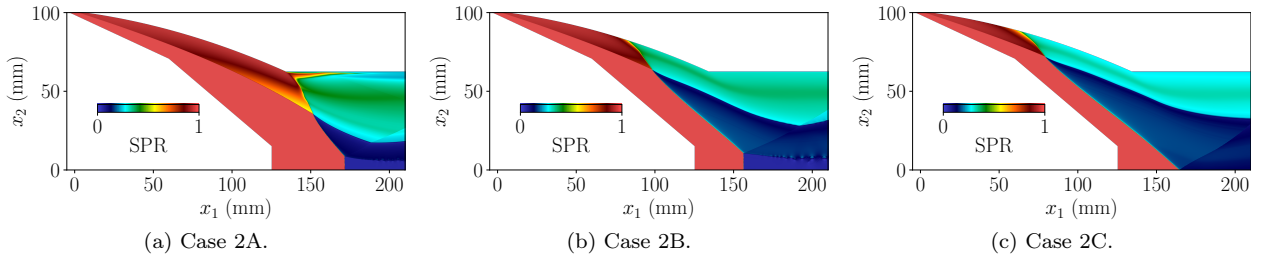

(a) Case 2A.

(b) Case 2B.

(c) Case 2C.

Figure 3.9: SPR distributions for Cases 2A, 2B, and 2C.

3.2.3. Case 3

This case corresponds to a higher curvature of $\kappa = 5.09$ km^{-1}, with Point C in Figure 2.1a moved upstream. In addition, because a larger domain is required, Point F is moved to $(-5, 0)$ mm, and Points G and H are removed (such that Points A and F are now connected via a line segment). Figures 3.10 and 3.11 display the temperature and pressure fields, respectively, for Cases 3A, 3B, and 3C at $t = 4.08$ ms, which is sufficiently long to reach a quasi-steady state. To reduce computational cost, each simulation is first run on a coarser mesh with characteristic element size $h = 0.2$ mm until approximately $t = 2.20$ ms. After uniform refinement of the mesh, such that the element size becomes $h = 0.1$ mm, the simulation is then continued until the final time is reached. An abrupt LSW-CDW transition and a Mach reflection pattern is observed in all cases. The height of the Mach stem is significantly greater than in Cases 1 and 2. The reflected shock originating from the secondary triple point reflects off the top horizontal wall. These shocks interact with the Kelvin-Helmholtz instabilities. Upon crossing the Mach stem, the flow becomes subsonic

12

and then accelerates as the secondary slip line is deflected downwards in the x_2-direction; after reaching sonic conditions, the flow accelerates further to supersonic speeds as the secondary slip line is deflected upwards.

Table 4 presents the LSW-CDW locations for each case. The addition of ozone shortens the initiation zone and moves the transition point upstream, though to a lesser degree than in the previous (lower-curvature) cases. Just as previously observed, the transitional detonation and transverse and reflected waves, as well as the CDW, are attenuated. Behind the combustion front and the CDW, the curvature of the wall induces noticeable compression in the ozonated cases. Such compression behind the combustion front and CDW is more prominent here than in Cases 1 and 2 because of the greater ramp angle, especially near the tail. In the ozone-free case, the region between the slip lines is significantly narrower than in Cases 3B and 3C, as a result of the taller Mach stem and larger initiation zone. There is almost no visible difference between Cases 3B and 3C (apart from the discrepancy in initiation length), which will be further discussed below.

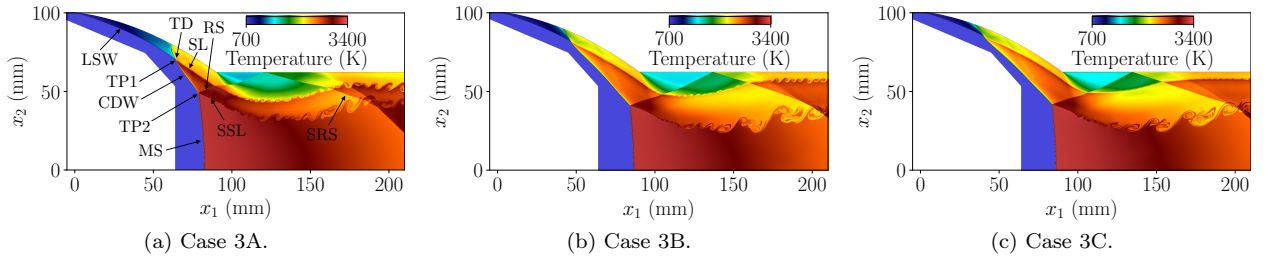(a) Case 3A.   (b) Case 3B.   (c) Case 3C.

Figure 3.10: Temperature fields for Cases 3A, 3B, and 3C. LSW: leading shock wave. TP1: transition point. TD: transitional detonation. CDW: curved detonation wave. SL: slip line. RS: reflected shock. MS: Mach stem. SSL: secondary slip line. TP2: secondary triple point. SRS: secondary reflected shock.
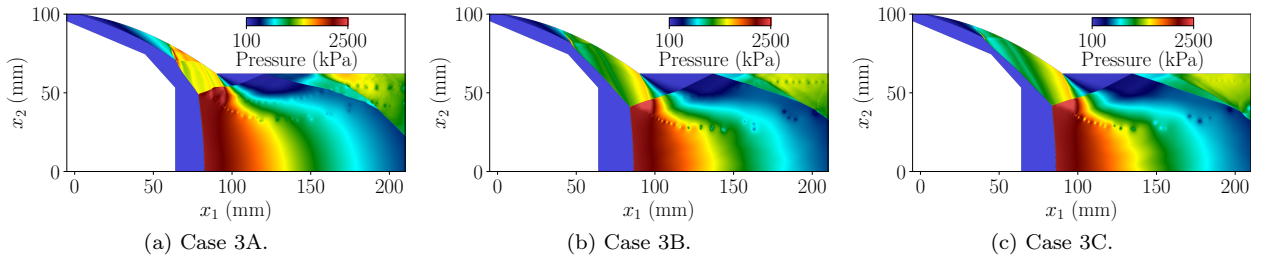

(a) Case 3A.   (b) Case 3B.   (c) Case 3C.

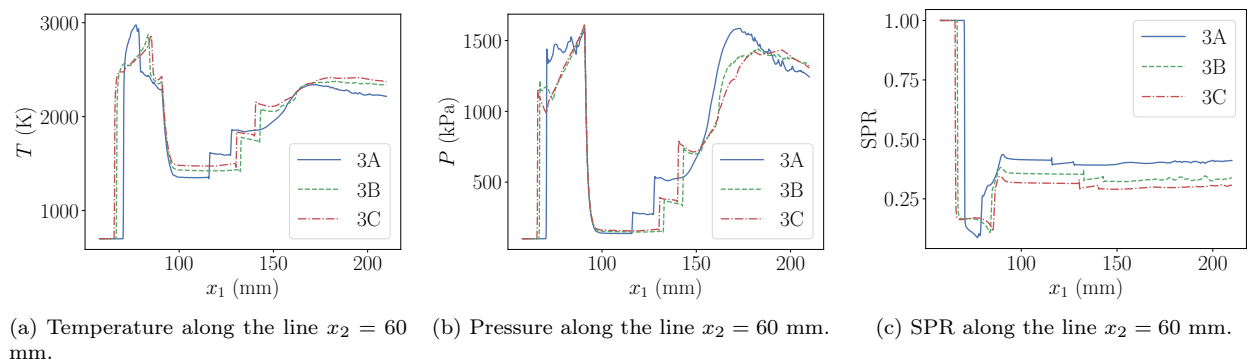Figure 3.11: Pressure fields for Cases 3A, 3B, and 3C.

Table 4: x_1-coordinates of LSW-CDW transitions for Case 3 (concave).

Case	Ozone addition	LSW-CDW transition	Relative change vs. Case 3A
3A	0 ppm	$x_1 \approx 64$ mm	0%
3B	1000 ppm	$x_1 \approx 47$ mm	27%
3C	10,000 ppm	$x_1 \approx 40$ mm	38%

Figures 3.12a and 3.12b present the variation of temperature and pressure, respectively, along the line $x_2 = 60$ mm, which intersects the CDW, slip line, reflected shock, and secondary reflected shock. The initial pressure and temperature jump is due to the CDW. Immediately behind the CDW, the overall increase in pressure is a result of compression induced by the concave wall, with the non-monotonicity of the pressure

13

profile caused by waves propagating from the initial reaction zone, which are especially noticeable in Case 3A. The expansion fan then leads to a large, rapid decrease in pressure. The next two jumps in pressure and temperature are caused by the reflected shock originating from the secondary triple point and the secondary reflected shock.

The difference between Cases 3A and 3B is considerably larger than the difference between Cases 3B and 3C. In contrast, in the lower-curvature Case 1 and Case 2, the difference between 1000 ppm of ozone and 10,000 ppm of ozone addition is still appreciable. To help explain this observation, we first compare Cases 3A and 3B. As shown in the pressure fields in Figure 3.11, even though the location of the transition does not change as significantly with 1000 ppm ozone addition as in Cases 1 and 2, there is a very noticeable difference in the LSW strengths at the transition point. This is because of the relatively large change in ramp angle in this high-curvature case (compared to Cases 1 and 2). When comparing Cases 3B and 3C, a difference in LSW strength at the transition point can still be discerned. However, due to the smaller reduction in initiation length, this difference is not as large and is eventually offset by the subsequent rapid continuous compression induced by the high-curvature ramp. On the other hand, this continuous compression behind the transition point is not sufficient to offset the difference between Cases 3A and 3B. These results illustrate the complex interactions among various competing effects in the case of curved walls (as opposed to straight-sided walls).

(a) Temperature along the line $x_2 = 60$ mm.

(b) Pressure along the line $x_2 = 60$ mm.

(c) SPR along the line $x_2 = 60$ mm.

Figure 3.12: Variation of temperature, pressure, and SPR along the line $x_2 = 60$ mm for Case 3 (concave).

The SPR distributions are presented in Figure 3.13. In all cases, the greatest loss in stagnation pressure occurs across the Mach stem. Consistent with previous results, the addition of ozone improves SPR across the CDW but reduces it behind the reaction zone above the slip line. This is further illustrated in Figure 3.12c, which shows the variation of SPR along the line $x_2 = 60$ mm.
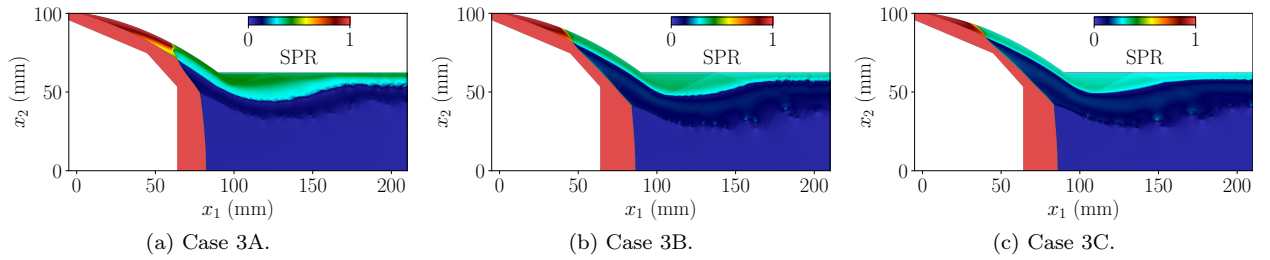

(a) Case 3A.

(b) Case 3B.

(c) Case 3C.

Figure 3.13: SPR distributions for Cases 3A, 3B, and 3C.

3.2.4. Case 4

14

The purpose of this case is to present a geometry for which the detonation is non-stationary in the absence of ozone but can be stabilized with ozone addition. Point C is moved upstream to $(84, 62)$ mm, leading to a mean curvature of $\kappa = 5.80$ km^{-1}, which is slightly larger than the mean curvature in Case 3. Each case is first computed on a coarser mesh with $h = 0.2$ mm until approximately $t = 2.20$ ms. The mesh is then uniformly refined, and the simulation is restarted. Figure 3.14 shows the temperature fields at $t = 4.15$ ms for Case 4A and $t = 4.24$ ms for Cases 4B and 4C. The temperature fields for Case 4B and 4C resemble those for Case 3B and 3C due to the similar geometries. However, in the absence of ozone, the detonation fails to stabilize. The Mach stem grows and accelerates towards the inflow boundary, and the CDW disappears. The reason for the non-stationary behavior is interaction between large high-pressure, subsonic regions in close proximity [30]. To illustrate, Figure 3.15 presents Mach-number distributions for Case 4A at three different points in time, where the subsonic regions are left uncolored. At earlier times, there is a subsonic region behind the reflected shock that eventually merges with the subsonic region behind the Mach stem, causing a non-stationary condition. Conversely, Figure 3.16 shows Mach-number distributions for Case 4C at three different points in time, where it is observed that the flow behind the reflected shock is nearly fully supersonic as a result of the detonation attenuation, preventing non-stationary behavior.

It should be noted, however, that the ability of ozone addition to stabilize a normally non-stationary detonation is limited, at least at the considered conditions. If Point C is moved marginally upstream to $(80, 62)$ mm, resulting in a mean curvature of $\kappa = 6.33$ km^{-1}, then ozone addition at concentrations of 1000 ppm and 10,000 ppm fail to stabilize the detonation (not shown for brevity). One potential reason is the very high ramp angle near the tail, which, as previously discussed, causes rapid post-transition compression that can appreciably counteract the benefits of a shortened initation zone. In the case of a non-stationary detonation with reduced continuous compression behind the combustion front and CDW, the ability of ozone addition to stabilize the detonation may be improved.
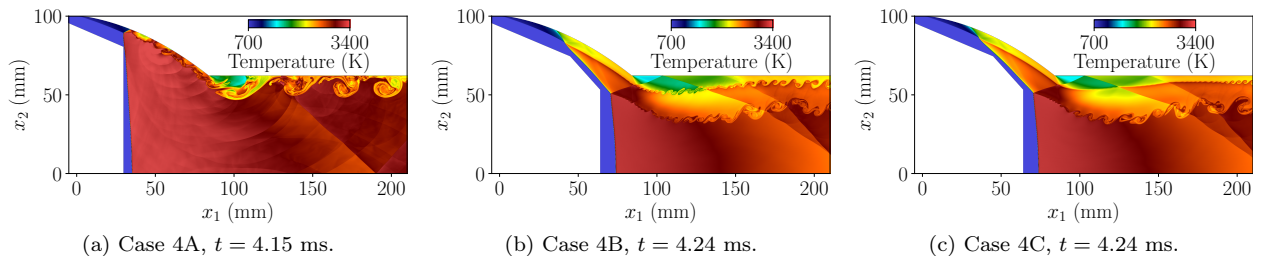

(a) Case 4A, $t = 4.15$ ms.   (b) Case 4B, $t = 4.24$ ms.   (c) Case 4C, $t = 4.24$ ms.

Figure 3.14: Temperature fields for Cases 4A, 4B, and 4C.

(a) $t = 2.51$ ms.   (b) $t = 3.77$ ms.   (c) $t = 4.15$ ms.
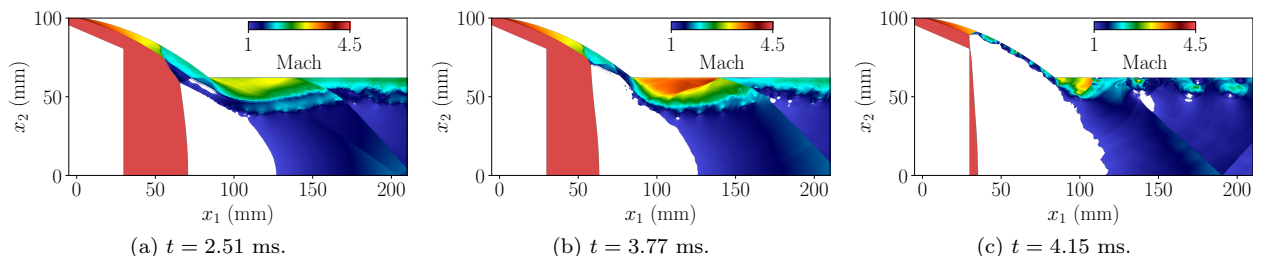
Figure 3.15: Mach-number distributions for Case 4A. Subsonic regions are left uncolored.

15

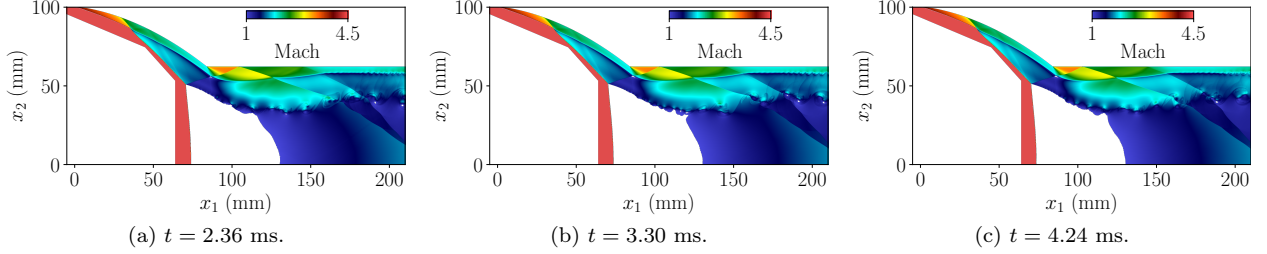(a) $t = 2.36$ ms.　　　　　　(b) $t = 3.30$ ms.　　　　　　(c) $t = 4.24$ ms.

Figure 3.16: Mach-number distributions for Case 4C. Subsonic regions are left uncolored.

3.3. Convex walls

Table 5 lists the two convex-wall cases considered in this study. α_2 is fixed across all cases, and Point C in Figure 2.1b is varied in the x_1-direction to obtain different curvatures. Case 1 corresponds to the highest curvature (in magnitude). At higher curvatures, the initiation length in the absence of ozone becomes very small, such that the effect of ozone addition is significantly reduced; therefore, higher curvatures are not considered. As indicated in the fifth column of Table 5, the letter refers to the ozone amount (e.g., Case 1C corresponds to $\kappa = -1.04$ km^{-1} and 10,000 ppm ozone). A regular reflection pattern is observed in all cases apart from Case 1A, which corresponds to a (stationary) Mach reflection, and Case 2A, in which the LSW fails to transition to a detonation.

Table 5: Geometric information for convex ramp. Units are in mm unless otherwise specified.

Case	Point C	Wall profile	κ $\left(\text{km}^{-1}\right)$	Ozone	Reflection pattern
1	$(150, 62)$	$x_{2,c} = 0.0005750x_1^2 - 0.3396x_1 + 100$	-1.04	1A: 0 ppm 1B: 1000 ppm 1C: 10,000 ppm	1A: Mach reflection 1B: Regular reflection 1C: Regular reflection
2	$(180, 52)$	$x_{2,c} = 0.0002446x_1^2 - 0.2551x_1 + 100$	-0.46	2A: 0 ppm 2B: 1000 ppm 2C: 10,000 ppm	2A: No detonation 2B: Regular reflection 2C: Regular reflection

3.3.1. Case 1

Figures 3.17 and 3.18 display the quasi-steady temperature and pressure fields, respectively, for Case 1A at $t = 1.57$ ms and Cases 1B and 1C at $t = 0.628$ ms. Case 1A is first computed on a coarser mesh with characteristic element size $h = 0.2$ mm until $t = 0.628$ ms, after which the mesh is uniformly refined (which yields $h = 0.1$ mm) and the simulation is continued until the final time. A regular reflection pattern is observed Case 1B and Case 1C, in which the LSW transitions to a CDW that then reflects off the bottom wall. Case 1A is instead characterized by a Mach reflection pattern, where the Mach stem is extremely small. Cellular structures are clearly observed in Cases 2B and 2C, while hints of a cellular structure can be discerned in Case 2A. Furthermore, in Case 2A, the induction zone ahead of the CDW noticeably increases in size downstream. In the absence of ozone, the LSW-CDW transition is abrupt. The addition of ozone reduces the initiation length and leads to a smooth transition, along with weakening or disappearance of the transverse waves originating from the LSW-CDW transition. In the vicinity of the transition point, the CDW is attenuated with ozone addition; however, as will be discussed below, the effect of ozone sensitization on the CDW away from the transition point (near the bottom wall) is more complicated. Due to the smaller initiation zone, the slip line is closer to the curved ramp. In Case 1A, the slip line intersects the reflected shock before the end of the domain. The difference between 0 ppm and 1000 ppm of ozone is greater than that between 1000 ppm and 10,000 ppm of ozone.

16

The x_1-coordinates of the LSW-CDW transitions, as well as the relative change with respect to the ozone-free case, are listed in Table 6. Despite the smaller initiation zone in the absence of ozone addition, the upstream relocation of the transition point is comparatively greater here than in the concave-ramp cases. The reason is that as the onset of combustion is moved upstream with greater ozone concentrations, the ramp angle increases, which has the amplifying effect of accelerating combustion. It should be noted, however, that this amplifying effect is not expected to be significant in this relatively low-curvature case. In the case of concave ramps, as previously discussed, the opposite is observed since the ramp angle instead decreases, thus mitigating combustion.
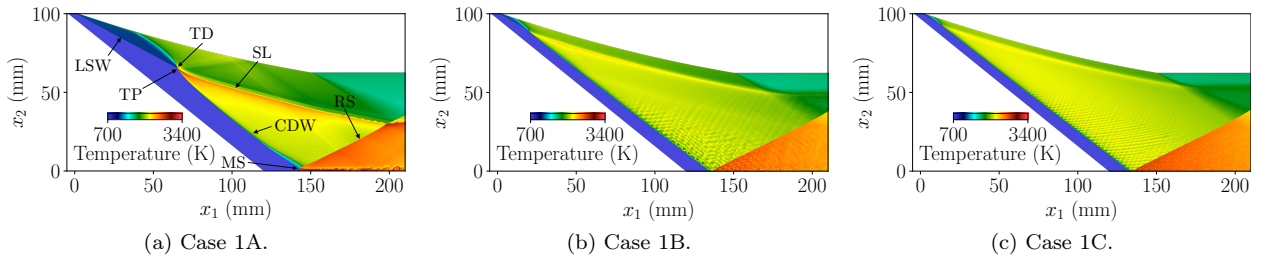

Figure 3.17: Temperature fields for Cases 1A, 1B, and 1C. LSW: leading shock wave. TP: transition point. TW: transverse wave. CDW: curved detonation wave. SL: slip line. RS: reflected shock.
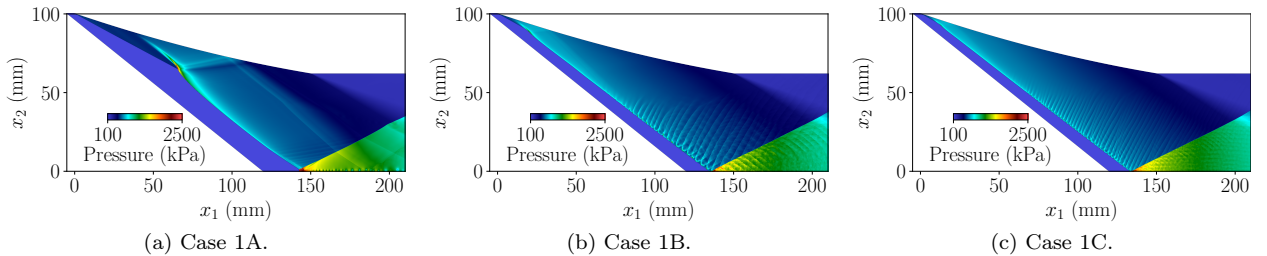

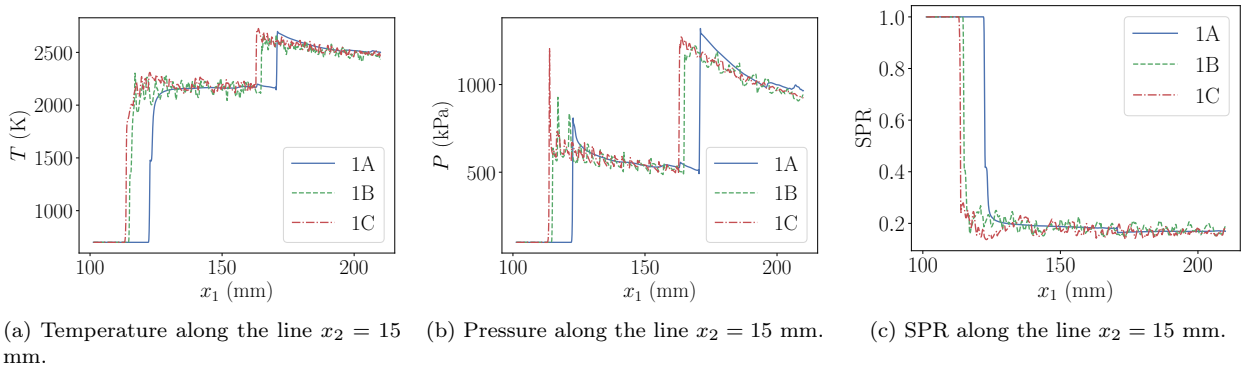Figure 3.18: Pressure fields for Cases 1A, 1B, and 1C.

Table 6: x_1-coordinates of LSW-CDW transitions for Case 1 (convex).

Case	Ozone addition	LSW-CDW transition	Relative change vs. Case 1A
1A	0 ppm	$x_1 \approx 66$ mm	0%
1B	1000 ppm	$x_1 \approx 21$ mm	68%
1C	10,000 ppm	$x_1 \approx 14$ mm	79%

Figures 3.19a and 3.19b presents the variation of temperature and pressure along the line $x_2 = 15$ mm, which intersects the CDW and the reflected shock. The oscillations in temperature and pressure are due to transverse waves associated with the cellular structure. The addition of ozone moves the CDW and reflected shock upstream. The first increase in temperature and pressure is a result of the CDW, and the second increase is due to the reflected shock. The gradual decreases in pressure behind the CDW and the reflected shock are caused by continuous expansion induced by the convex wall.

In the case of ODWs, ozone addition often attenuates the detonation, especially if the transition type changes from abrupt to smooth [21, 22] (which is the case here), leading to improved propulsion performance.

17

For convex ramps, however, there is a competing effect wherein a shorter initiation zone leads to a stronger shock at the transition point (due to a greater ramp angle). Here, this competing effect slightly offsets the smoothening of the LSW-CDW transition, such that far away from the transition point, the temperature behind the CDW in Case 1C (10,000 ppm of ozone) is overall slightly greater than in Case 1A (no ozone). However, given the relatively low curvature, this competing effect is not expected to be significant, especially since another contributing factor to the higher overall post-CDW temperature in Case 1C is that ozone addition already leads to slightly greater post-detonation temperatures in the one-dimensional ZND setting (as in Section 3.1).

(a) Temperature along the line $x_2 = 15$ mm.

(b) Pressure along the line $x_2 = 15$ mm.

(c) SPR along the line $x_2 = 15$ mm.

Figure 3.19: Variation of temperature, pressure, and SPR along the line $x_2 = 15$ mm for Case 1 (convex).

Figure 3.20 shows the distributions of SPR. The post-reaction region above the slip line exhibits higher SPR in the absence of ozone additive. This is because ozone sensitization, by way of shortening the initiation zone, mitigates the coalescence of compression waves along the combustion front [21], and stronger compression in the reaction zone improves the SPR [29]. Greater stagnation-pressure losses are observed across the CDW, especially near the transition point where the detonation is strongest. Additional loss in stagnation pressure occurs across the reflected shock. Near the transition point, ozone addition improves SPR across the CDW, which is consistent with the ODW setting [21]. However, away from the transition point (near the bottom wall), stagnation-pressure loss across the CDW is highest in Case 1C (10,000 ppm of ozone), as Figure 3.19c shows. The overall greatest stagnation-pressure loss is observed behind the Mach stem in Case 1A.
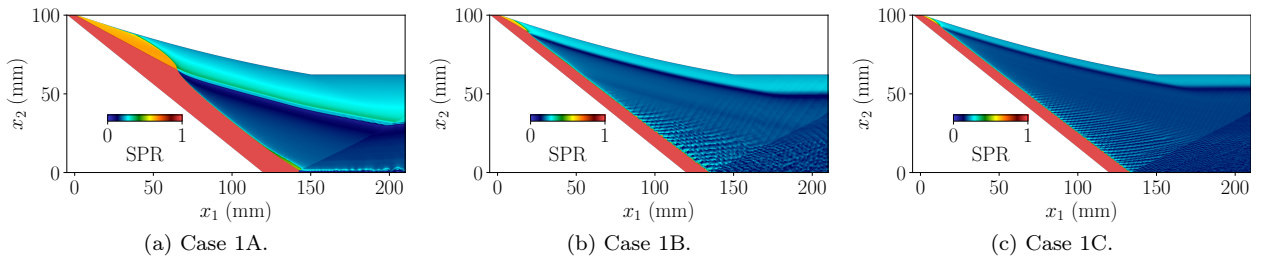

(a) Case 1A.

(b) Case 1B.

(c) Case 1C.

Figure 3.20: SPR distributions for Cases 1A, 1B, and 1C.

3.3.2. Case 2

This case corresponds to a very low mean curvature of $\kappa = -0.46$ km^{-1}, such that the ramp is nearly linear. Figures 3.21 and 3.22 present the temperature and pressure fields, respectively, at $t = 0.628$ ms. In the absence of ozone, the LSW fails to transition to a detonation. With ozone addition, shock-detonation transition occurs, and a regular reflection pattern is observed. Table 7 provides the transition locations.

18

Cellular structures are apparent in Cases 2B and 2C. It is worth noting that the difference between 1000 ppm ozone and 10,000 ppm ozone is greater here than in the concave-ramp cases (at least in terms of transition-point relocation), again due to additional effects induced by the ramp concavity. Compared to Case 2B, the transition point in Case 2C is moved upstream, the transverse waves are weaker, and the slip line is closer to the convex ramp.
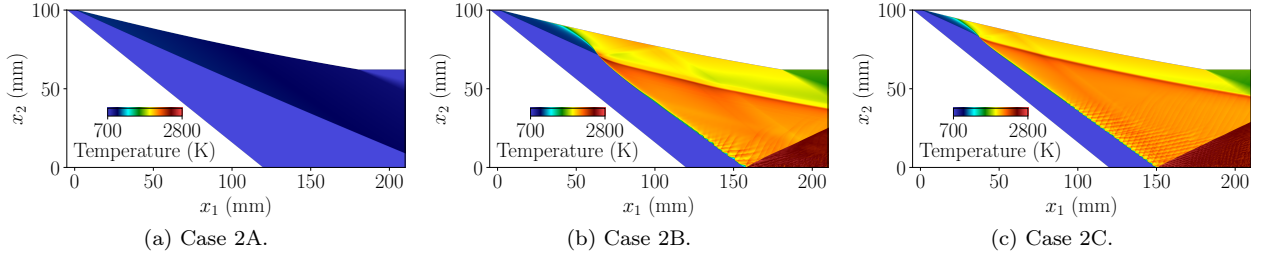

(a) Case 2A.   (b) Case 2B.   (c) Case 2C.

Figure 3.21: Temperature fields for Cases 2A, 2B, and 2C.

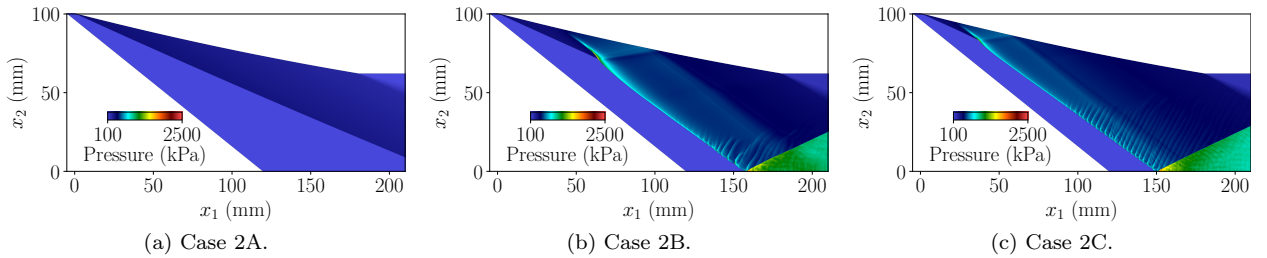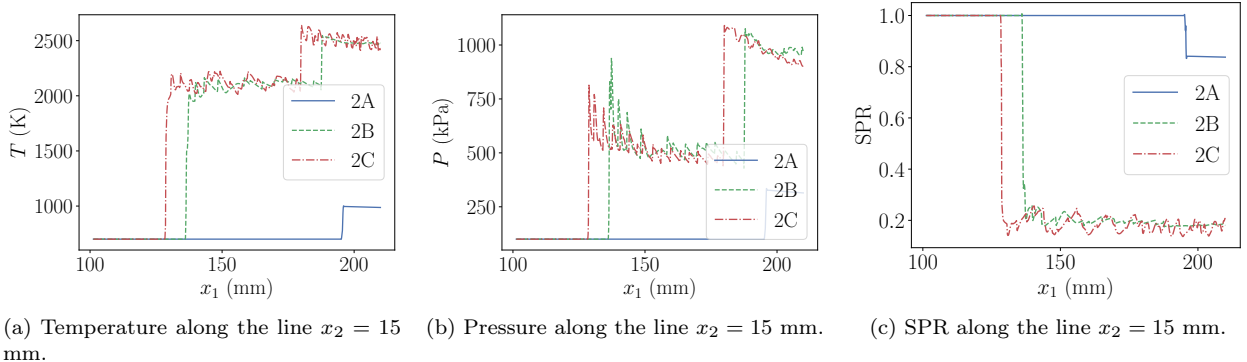(a) Case 2A.   (b) Case 2B.   (c) Case 2C.

Figure 3.22: Pressure fields for Cases 2A, 2B, and 2C.

Table 7: x_1-coordinates of LSW-CDW transitions for Case 1 (convex).

Case	Ozone addition	LSW-CDW transition	Relative change vs. Case 2B
2A	0 ppm	n/a	n/a
2B	1000 ppm	$x_1 \approx 64$ mm	0%
2C	10,000 ppm	$x_1 \approx 37$ mm	42%

Figures 3.23a and 3.23b show the variation of temperature and pressure, respectively, along the line $x_2 = 15$ mm. In Case 2A, this line sampler intersects the LSW, while in Cases 2B and 2C, it intersects the CDW and reflected shock. The temperature and pressure oscillations are again due to the transverse waves associated with the cellular structure. In Cases 2B and 2C, the first large jump in temperature and pressure is due to the CDW, and the second is due to the reflected shock. Expansion due to the ramp convexity and the convex corner is also observed. Compared to Case 2B, the CDW and reflected shock in Case 2C are located further upstream. Apart from the different CDW and reflected-shock locations, the temperature, pressure, and SPR profiles are overall similar between Cases 2B and 2C. SPR is of course highest in Case 2A since the LSW fails to even transition to a detonation.

19

(a) Temperature along the line $x_2 = 15$ mm.

(b) Pressure along the line $x_2 = 15$ mm.

(c) SPR along the line $x_2 = 15$ mm.

Figure 3.23: Variation of temperature, pressure, and SPR along the line $x_2 = 15$ mm for Case 2 (convex).

4. Concluding remarks

CDWs induced by curved ramps represent a promising, relatively new standing-detonation-engine concept. We performed two-dimensional simulations of CDWs in a confined combustion chamber and examined the effect of ozone sensitization on their reflection patterns and flow characteristics. The main findings are as follows:

- Just as for ODWs, ozone addition reduces the size of the initiation zone and can change the LSW-CDW transition type from abrupt to smooth. The overall effect of ozone addition is typically greater in cases with large initiation zones in the absence of ozone. The use of curved ramps introduces complexities that can lead to additional competing effects not present in the ODW setting.

- In the case of concave walls, the reduction of the initiation length causes the LSW-CDW transition to move upstream, where the LSW is shallower and weaker. This somewhat offsets the ozone-induced decrease in initiation length since the region with greater ramp angles (and thus greater compression) is no longer spanned by the initiation zone. At the same time, the detonation-attenuation effect associated with smoothening of the LSW-CDW transition is magnified, again due to the shallower ramp angle at the transition point. Ozone addition can thus reduce stagnation-pressure losses across the CDW and improve detonation stabilization. In particular, it was observed that ozone addition can change a non-stationary Mach reflection pattern to a stationary Mach reflection pattern and a stationary Mach reflection pattern to a regular reflection pattern. However, for high mean curvatures, the large ramp angle near the tail of the ramp can cause significant continuous compression behind the LSW-CDW transition that then mitigates the detonation-attenuation effect. Finally, the higher-Mach-number flow behind the CDW can reduce or eliminate the Mach stem, thus further reducing stagnation-pressure losses.

- In the case of convex walls, the reduction of the initiation length causes the LSW-CDW transition to similarly move upstream, where the LSW is instead steeper and stronger. The initiation zone is thus shortened to a greater extent than in the case of concave walls. The CDW can possibly be strengthened, which is in direct competition with smoothening of the LSW-CDW transition. If strengthening of the CDW is the dominant effect, then propulsion performance and detonation stabilization may be detrimentally affected. However, it should be noted that the overall effect on SPR, which is a measure of propulsion performance, is not observed to be significant (also the case for concave ramps).

This study contributes to improved understanding of standing CDWs and ozone sensitization. Future work may investigate the effect of ozone addition on CDWs at a wider range of conditions (e.g., additional flight Mach numbers, different chamber dimensions/configurations, and more complex ramp shapes, such as ramps that change in convexity [29, 30]). Viscous effects will also be considered.

Acknowledgments

References

[1] K. Kailasanath, Review of propulsion applications of detonation waves, AIAA Journal 38 (9) (2000) 1698–1708.

[2] K. Kailasanath, Recent developments in the research on pulse detonation engines, AIAA Journal 41 (2) (2003) 145–159.

[3] K. Kailasanath, The rotating detonation-wave engine concept: a brief status report, in: 49th AIAA aerospace sciences meeting including the new horizons forum and aerospace exposition, 2011, p. 580.

[4] A. K. Gupta, D. A. Schwer, Rotating detonation engine concept: direct combustion of supersonic inflow, Journal of Propulsion and Power 34 (2) (2018) 562–564.

[5] W. H. Heiser, D. T. Pratt, Thermodynamic cycle analysis of pulse detonation engines, Journal of Propulsion and Power 18 (1) (2002) 68–76.

[6] P. Wolański, Detonation engines, Journal of KONES 18 (3) (2011) 515–521.

[7] D. A. Rosato, M. Thornton, J. Sosa, C. Bachman, G. B. Goodwin, K. A. Ahmed, Stabilized detonation for hypersonic propulsion, Proceedings of the National Academy of Sciences 118 (20) (2021) e2102244118.

[8] D. T. Pratt, J. W. Humphrey, D. E. Glenn, Morphology of standing oblique detonation waves, Journal of Propulsion and Power 7 (5) (1991) 837–845.

[9] C. Li, K. Kailasanath, E. S. Oran, Detonation structures behind oblique shocks, Physics of Fluids 6 (4) (1994) 1600–1611.

[10] C. Viguier, L. F. F. Da Silva, D. Desbordes, B. Deshaies, Onset of oblique detonation waves: Comparison between experimental and numerical results for hydrogen-air mixtures, in: Symposium (International) on Combustion, Vol. 26, Elsevier, 1996, pp. 3023–3031.

[11] A.-F. Wang, W. Zhao, Z.-L. Jiang, The criterion of the existence or inexistence of transverse shock wave at wedge supported oblique detonation wave, Acta Mechanica Sinica 27 (2011) 611–619.

[12] H. H. Teng, Z. L. Jiang, On the transition pattern of the oblique detonation structure, Journal of Fluid Mechanics 713 (2012) 659–669.

[13] T. Wang, Y. Zhang, H. Teng, Z. Jiang, H. D. Ng, Numerical study of oblique detonation wave initiation in a stoichiometric hydrogen-air mixture, Physics of Fluids 27 (9) (2015).

[14] Y. Liu, L. Wang, B. Xiao, Z. Yan, C. Wang, Hysteresis phenomenon of the oblique detonation wave, Combustion and Flame 192 (2018) 170–179.

[15] J.-Y. Choi, D.-W. Kim, I.-S. Jeung, F. Ma, V. Yang, Cell-like structure of unstable oblique detonation wave from high-resolution numerical simulation, Proceedings of the Combustion Institute 31 (2) (2007) 2473–2480.

[16] J. Verreault, A. J. Higgins, R. A. Stowe, Formation of transverse waves in oblique detonations, Proceedings of the Combustion Institute 34 (2) (2013) 1913–1920.

[17] H. Teng, H. D. Ng, K. Li, C. Luo, Z. Jiang, Evolution of cellular structures on oblique detonation surfaces, Combustion and Flame 162 (2) (2015) 470–477.

[18] S. Ramachandran, S. Yang, Micro-jetting and transverse waves in oblique detonations, Combustion and Flame 265 (2024) 113506.

[19] A. E. Magzumov, I. A. Kirillov, V. D. Rusanov, Effect of small additives of ozone and hydrogen peroxide on the induction-zone length of hydrogen-air mixtures in a one-dimensional model of a detonation wave, Combustion, Explosion and Shock Waves 34 (1998) 338–341.

[20] J. Crane, X. Shi, A. V. Singh, Y. Tao, H. Wang, Isolating the effect of induction length on detonation structure: Hydrogen–oxygen detonation promoted by ozone, Combustion and Flame 200 (2019) 44–52.

[21] H. Teng, S. Liu, Z. Li, P. Yang, K. Wang, C. Tian, Effect of ozone addition on oblique detonations in hydrogen-air mixtures, Applied Thermal Engineering 240 (2024) 122292.

[22] A. Vashishtha, S. Panigrahy, D. Campi, D. Callaghan, C. Nolan, R. Deiterding, Oblique detonation wave control with O3 and H2O2 sensitization in hypersonic flow, Energies 15 (11) (2022) 4140.

[23] J. Verreault, A. J. Higgins, R. A. Stowe, Formation and structure of steady oblique and conical detonation waves, AIAA journal 50 (8) (2012) 1766–1772.

[24] P. Yang, H. D. Ng, H. Teng, Z. Jiang, Initiation structure of oblique detonation waves behind conical shocks, Physics of Fluids 29 (8) (2017).

[25] W. Han, C. Wang, C. K. Law, Three-dimensional simulation of oblique detonation waves attached to cone, Physical Review Fluids 4 (5) (2019) 053201.

[26] L. Zhou, S. Tu, Y. Zhang, P. Yang, H. Teng, Numerical investigation of oblique detonation waves on a truncated cone in hydrogen–air mixtures, Physics of Fluids 35 (11) (2023).

[27] T. Honghui, Y. Zhang, Y. Pengfei, Z. Jiang, Oblique detonation wave triggered by a double wedge in hypersonic flow, Chinese Journal of Aeronautics 35 (4) (2022) 176–184.

[28] G. Xiang, Y. Zhang, Q. Tu, Y. Gao, X. Huang, T. Peng, The initiation characteristics of oblique detonation waves induced by a curved surface, Aerospace Science and Technology 128 (2022) 107743.

[29] H. Xiong, R. Qiu, X. Han, H. Yan, Y. You, Investigating the flow characteristics and thermodynamic performance of curved detonation waves, Physics of Fluids 35 (8) (2023).

[30] H. Yan, X. Han, H. Xiong, C. Shi, Y. You, Curved detonation and its reflections, Journal of Fluid Mechanics 984 (2024) A11.

[31] K. Wang, Z. Zhang, P. Yang, H. Teng, Numerical study on reflection of an oblique detonation wave on an outward turning wall, Physics of Fluids 32 (4) (2020).

[32] Z. Zhang, Y. Liu, C. Wen, Mechanisms of the destabilized Mach reflection of inviscid oblique detonation waves before an expansion corner, Journal of Fluid Mechanics 940 (2022) A29.

[33] B. J. McBride, S. Gordon, M. A. Reno, Coefficients for calculating thermodynamic and transport properties of individual species (1993).

[34] B. J. McBride, M. J. Zehe, S. Gordon, NASA Glenn coefficients for calculating thermodynamic properties of individual species (2002).

[35] G. P. Smith, Y. Tao, H. Wang, Foundational fuel chemistry model version 1.0 (FFCM-1), `http://nanoenergy.stanford.edu/ffcm1` (2016).

[36] H. Zhao, X. Yang, Y. Ju, Kinetic studies of ozone assisted low temperature oxidation of dimethyl ether in a flow reactor using molecular-beam mass spectrometry, Combustion and Flame 173 (2016) 187–194.

[37] E. J. Ching, R. F. Johnson, A. D. Kercher, Positivity-preserving and entropy-bounded discontinuous Galerkin method for the chemically reacting, compressible Euler equations. Part I: The one-dimensional case, Journal of Computational Physics (2024) 112881.

[38] E. J. Ching, R. F. Johnson, A. D. Kercher, Positivity-preserving and entropy-bounded discontinuous Galerkin method for the chemically reacting, compressible Euler equations. Part II: The multidimensional case, Journal of Computational Physics (2024) 112878.

[39] R. F. Johnson, A. D. Kercher, A conservative discontinuous Galerkin discretization for the chemically reacting Navier–Stokes equations, Journal of Computational Physics 423 (2020) 109826. `doi:10.1016/j.jcp.2020.109826`.

[40] S. Gottlieb, C. Shu, E. Tadmor, Strong stability-preserving high-order time discretization methods, SIAM review 43 (1) (2001) 89–112.

[41] D. I. Ketcheson, Highly efficient strong stability-preserving runge–kutta methods with low-storage implementations, SIAM Journal on Scientific Computing 30 (4) (2008) 2113–2136.

[42] E. Ching, Y. Lv, P. Gnoffo, M. Barnhardt, M. Ihme, Shock capturing for discontinuous Galerkin methods with application to predicting heat transfer in hypersonic flows, Journal of Computational Physics 376 (2019) 54–75.

[43] P.-O. Persson, Shock capturing for high-order discontinuous Galerkin simulation of transient flow problems, in: 21st AIAA Computational Fluid Dynamics Conference, 2013, p. 3061.

[44] R. Hartmann, P. Houston, An optimal order interior penalty discontinuous Galerkin discretization of the compressible Navier–Stokes equations, Journal of Computational Physics 227 (22) (2008) 9670–9685.

[45] C. Geuzaine, J.-F. Remacle, Gmsh: a three-dimensional finite element mesh generator with built-in pre- and post-processing facilities, International Journal for Numerical Methods in Engineering (79(11)) (2009) 1310–1331.

[46] J. E. Shepherd, Explosion dynamics laboratory: Shock and detonation toolbox - 2018 version, jES 9-19-2018 (2018). URL `http://shepherd.caltech.edu/EDL/PublicResources/sdt/`

Appendix A. Grid convergence

Appendix A.1. Concave walls

Grid convergence is assessed on Case 4C, which corresponds to the smallest initiation zone across all (stationary) concave-ramp cases. Three mesh sizes are considered: $h = 0.2$ mm (Mesh 1), $h = 0.1$ mm (Mesh 2), and $h = 0.05$ mm (Mesh 3). Note that with a $p = 1$ solution approximation, each triangular element has three degrees of freedom (per state variable). We first compute this case on Mesh 1 up to $t = 2.20$ ms. The solution is uniformly refined (which corresponds to Mesh 2) and then computed up to $t = 4.24$ ms. Finally, after another level of uniform refinement (Mesh 3), the simulation is continued until $t = 7.92$ ms. A quasi-steady state is achieved on each mesh. Figures A.1 and A.2 provide the final temperature and pressure fields, respectively. The Kelvin-Helmholtz instabilities along the lower (secondary) slip line exhibit smaller-scale features with the finer meshes. Along the upper slip line, the Kelvin-Helmholtz instabilities are most noticeable on Mesh 3; on Mesh 1, they do not appear at all. Nevertheless, the overall reflection pattern is consistent across all meshes.
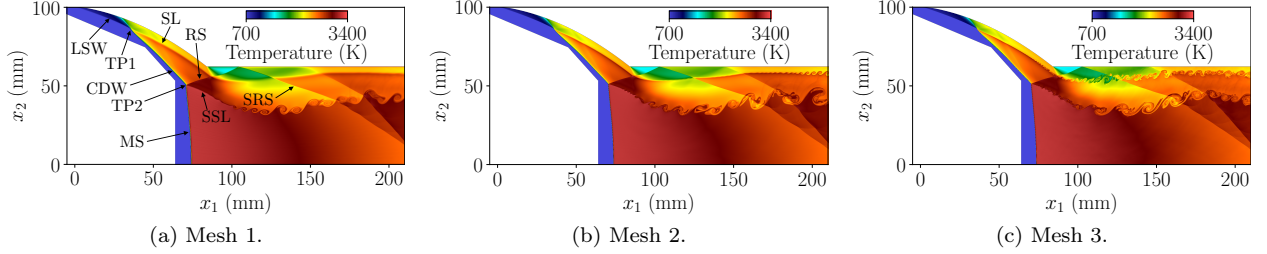
Figure A.1: Temperature fields for Case 1C with different meshes. Mesh 1: $h = 0.2$ mm. Mesh 2: $h = 0.1$ mm. Mesh 3: $h = 0.05$ mm. LSW: leading shock wave. TP1: transition point. CDW: curved detonation wave. SL: slip line. RS: reflected shock. MS: Mach stem. SSL: secondary slip line. TP2: secondary triple point. SRS: secondary reflected shock.
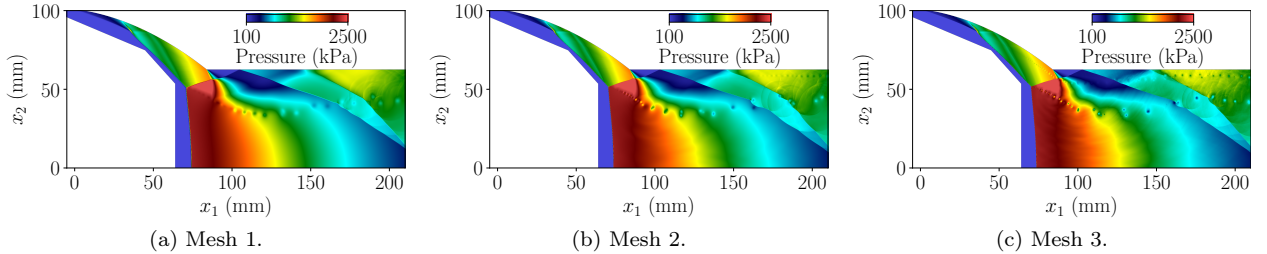

Figure A.2: Pressure fields for Case 1C with different meshes. Mesh 1: $h = 0.2$ mm. Mesh 2: $h = 0.1$ mm. Mesh 3: $h = 0.05$ mm.

Figure A.3a presents the variation of temperature along the line $x_2 = 68$ mm, which intersects the CDW front and the slip line. Smearing of the CDW front and slip line is most evident on Mesh 1. Figure A.3b zooms in on the vicinity of the slip line, across which a sharp decrease in temperature occurs. The peak temperature immediately before the slip line increases as the mesh is refined. Figure A.3c shows the temperature variation along $x_2 = 8$ mm, which intersects the Mach stem. As illustrated in the close-up view in Figure A.3d, the Mach-stem location is moved upstream as the resolution is increased. On the whole, the temperature profiles for Mesh 2 and Mesh 3 are very similar. Despite a slight underprediction of the peak temperature in Figure A.3a, Mesh 2 ($h = 0.1$ mm) is deemed to be sufficient to capture the overall reflection patterns and flow characteristics of interest and is therefore used for the simulations in Section 3.2.
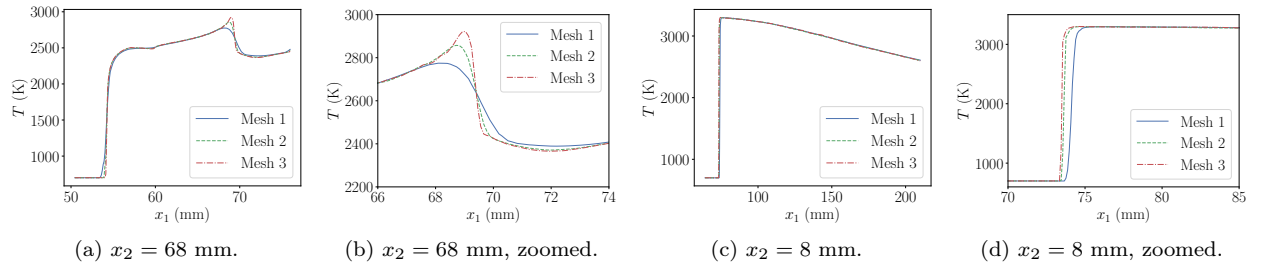

Figure A.3: Variation of temperature along the lines $x_2 = 68$ mm and $x_2 = 8$ mm. Zoomed-in views are also provided. Mesh 1: $h = 0.2$ mm. Mesh 2: $h = 0.1$ mm. Mesh 3: $h = 0.05$ mm.

Appendix A.2. Convex walls

Grid convergence is assessed on Case 1C, which corresponds to the smallest initiation zone across all convex-ramp cases. Three characteristic mesh sizes are considered: $h = 0.2$ mm (Mesh 1), $h = 0.1$ mm

(Mesh 2), and $h = 0.05$ mm (Mesh 3). The final time for the Mesh 1 and Mesh 2 solutions is $t = 0.627$ ms. The Mesh 3 solution is obtained by uniformly refining the Mesh 2 solution and restarting the simulation, with a final time of $t = 0.785$ ms. A quasi-steady state is achieved in all cases. Figures A.4 and A.5 present the final temperature and pressure fields, respectively. In all cases, the LSW transitions into a CDW that reflects off the bottom wall. A cellular structure along the CDW front appears with Mesh 2 and especially Mesh 3, but not with Mesh 1. It should be noted that the grid is likely not converged with respect to the cellular structure since mesh sizes approaching the mean free path may be required [18]. Nevertheless, this study is concerned with the overall reflection patterns, which are similar across all meshes, so accurate resolution of the cellular structure is not required; indeed, in related studies, the mesh resolution often is not sufficiently fine for a cellular structure to appear [21, 22, 30].

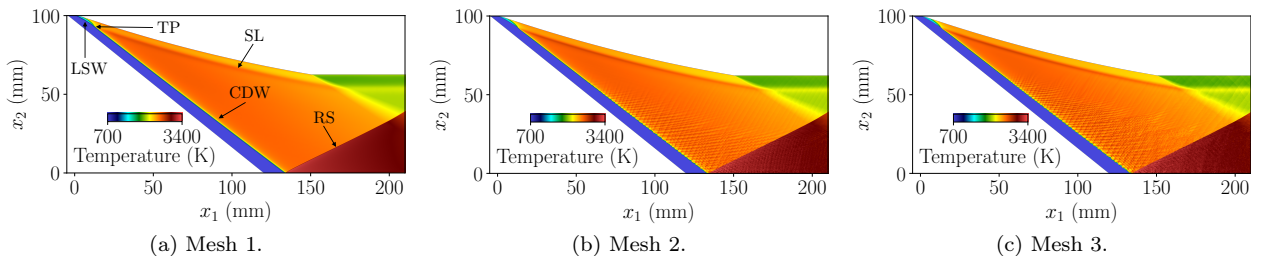

| (a) Mesh 1. | (b) Mesh 2. | (c) Mesh 3. |

Figure A.4: Temperature fields for Case 2C with different meshes. Mesh 1: $h = 0.2$ mm. Mesh 2: $h = 0.1$ mm. Mesh 3: $h = 0.05$ mm. LSW: leading shock wave. CDW: curved detonation wave. SL: slip line. RS: reflected shock. TP: transition point.

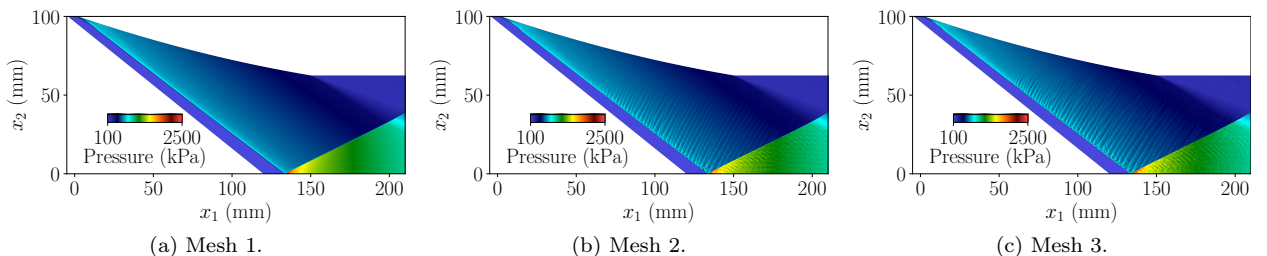| (a) Mesh 1. | (b) Mesh 2. | (c) Mesh 3. |

Figure A.5: Pressure fields for Case 2C with different meshes. Mesh 1: $h = 0.2$ mm. Mesh 2: $h = 0.1$ mm. Mesh 3: $h = 0.05$ mm.

For a more detailed assessment of grid convergence (with respect to the global wave structure), Figure A.6a presents the variation of temperature along the line $x_2 = 80$ mm, which intersects the CDW and the slip line. The temperature profile in the vicinity of the slip line is diffused with Mesh 1, and the peak temperature is somewhat underpredicted. Figure A.6b zooms in on the CDW front, where the finer meshes lead to a sharper profile. In addition, with Mesh 3, an induction zone can be discerned. Nevertheless, there is good agreement among the temperatures behind the CDW front and the CDW locations. Figure A.6c shows the temperature variation along $x_2 = 59$ mm, which additionally intersects the expansion fan around the convex corner. The temperature oscillations for Mesh 3 are due to the transverse waves associated with the cellular structure. As illustrated in the zoomed-in view presented in Figure A.6d, the finer meshes yield a sharper temperature profile and slightly higher peak temperature in the vicinity of the slip line. Given these results, Mesh 2 ($h = 0.1$ mm) is deemed to be sufficient to capture the overall reflection patterns and flow characteristics of interest and is therefore used for the simulations in Section 3.3.

24

(a) $x_2 = 80$ mm.   (b) $x_2 = 80$ mm, zoomed.   (c) $x_2 = 59$ mm.   (d) $x_2 = 59$ mm, zoomed.
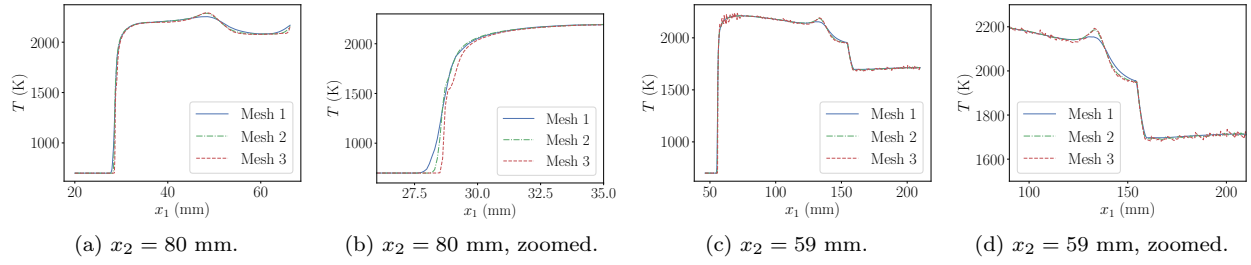
Figure A.6: Variation of temperature along the lines $x_2 = 80$ mm and $x_2 = 59$ mm. Zoomed-in views are also provided. Mesh 1: $h = 0.2$ mm. Mesh 2: $h = 0.1$ mm. Mesh 3: $h = 0.05$ mm.